RSC Advances

PAPER

View Article Online
View Journal | View Issue

Cite this: *RSC Adv.*, 2024, **14**, 14080

Investigating the influence of Cu and Ti substitution on the structural, optical, and dielectric properties of $BiFeO_3$

A. Ouertani,[a] Z. Abdelkafi, *[a] H. Khemakhem[a] and N. Randrianantoandro[b]

The environmentally friendly $BiFe_{1-x}(Ti_{1/2}Cu_{1/2})_xO_3$ system with various substitution rates, including $x = 0$ (BFO), $x = 0.02$ ($BFTCO_2$) and $x = 0.04$ ($BFTCO_4$), has been synthesized using the solid-state reaction technique. All compositions exhibited a distorted rhombohedral structure with *R*3*c* space, as observed from the results of XRD and Raman spectroscopy. A significant impurity phase ($Bi_{25}FeO_{40}$) appears in pure and doped BFO, with a percentage ranging between 6 and 9%. This impurity was also detected using Mössbauer spectroscopy. UV-vis spectroscopy revealed a decrease in optical band energy with the substitution, suggesting the potential applications of doped BFO within the visible range of the spectrum, making it suitable for photocatalytic and solar cell applications. The smallest bandgap was observed for $BFTCO_2$ with $E_g = 1.93$ eV. The origin of this reduction is discussed from a scientific point of view. Furthermore, Cu^{2+} and Ti^{4+} co-doped BFO display an improvement in dielectric properties due to the reduction in the value of tan δ. Dielectric measurements revealed an anomaly below T_N with diffusive and dispersive behavior, suggesting a relaxor-like behavior for all compositions. The relaxor character was quantified by using the Vogel–Fulcher relationship which yielded activation energy of 0.359–0.614 eV. In our system, the relaxor behavior showed an enhancement with the heterogeneity created by the substitution rate, reaching its maximum for $BFTCO_4$, characterized by the empirical parameters which are: $\Delta T_{relax} = 96$ K and $\gamma = 1.96$. Finally, co-doped BFO ceramics not only present promising materials for optical applications due to the narrow bandgap, but their relaxor behavior can also be tailored for promising applications in high-energy storage devices.

Received 10th March 2024
Accepted 22nd April 2024

DOI: 10.1039/d4ra01850h

rsc.li/rsc-advances

1. Introduction

Materials that exhibit the coexistence of ferroic orders, including ferroelectric and (anti)ferromagnetic properties, are referred to as multiferroics. These materials hold promise for diverse device applications like memory, microelectronics and spintronics.[1,2] In this respect, $BiFeO_3$ (BFO), the most well-known multiferroic, is one of the rare materials that exhibit the coexistence of antiferromagnetic and ferroelectric orders at room temperature (RT). BFO boasts a high Curie temperature ($T_C = 1103$ K) and a high Néel temperature ($T_N = 643$ K).[3,4] In its bulk form, the crystal structure stabilizes in a rhombohedral configuration with the *R*3*c* space group. Ferroelectricity arises from the distortion induced by stereochemically active $6s^2$ lone pair electrons of Bi^{3+}, while the indirect magnetic exchange interaction between Fe^{3+} ions through O^{2-} causes G-type antiferromagnetic ordering. This ordering is superimposed with a space-modulated spiral structure of an incommensurate wavelength of 62 nm.[5] However, this structure is responsible for the suppression of weak ferromagnetism and the linear magneto-electric (M-E) effect.[6] Additionally, synthesizing a single-phase BFO is a challenging task due to several factors such as oxygen vacancies, mixed valence states of Fe ions, and impurity phases like $Bi_{25}FeO_{40}$, which enhance electrical conductivity, posing a serious drawback for device applications.[7] To mitigate these issues and reduce leakage currents, various attempts have been made, including adopting different processing techniques,[8–10] substituting elements at the Bi/Fe site,[10,11] and fabricating composites.[12]

On the other hand, BFO stands out as a promising lead-free ferroelectric material, owing to its exceptional intrinsic polarization exceeding 100 μC cm^{-2}.[13] Generally, polarization can remain stable across various temperatures in relaxors due to their diffuse phase transition behavior near dielectric maxima. This behavior holds a significant promise in several applications such as sensors, capacitors, actuators, piezoelectric transducers and notably in dielectric energy storage applications.[14–16] Doping at site A or B emerges as an effective strategy to achieve a more diffuse transition phase by modifying

[a]*Laboratory of Multifunctional Materials and Applications (LaMMA), LR16ES18, Faculty of Sciences of Sfax, University of Sfax, B.P. 1171, Sfax, 3000, Tunisia. E-mail: zied_abdelkafi@yahoo.fr*

[b]*Institut des Molécules et Matériaux du Mans – UMR 6283, CNRS – Le Mans Université, Avenue Olivier Messaien, Le Mans, 72085, France*

the short-range ordering nature due to the difference in size and charge between host and dopant elements.[17,18]

Furthermore, BFO has recently gained significant attention for its potential application in photolysis and photocatalytic activity due to its smaller bandgap (ranging between 1.9 eV and 2.8 eV at RT[19–22]) in comparison to other ferroelectric oxides like $BaTiO_3$, $LiNbO_3$, and $PbZrTiO_3$ (with a bandgap of $E_g > 3$ eV). Therefore, reducing the bandgap further becomes essential for enhanced absorption of the larger part of the sunlight spectrum, particularly in the visible range. Substitution is a potential approach to further reduce this gap as observed in Ti-doped BFO,[23,24] (Cu, Zr) co-doped BFO[25] and (Zr, Zn) co-doped BFO.[26]

Several studies suggest that doping with 4+ ions is anticipated to decrease the formation of oxygen vacancies, while the introduction of 2+ ions is expected to hinder the creation of Fe^{2+} ions.[27] In this context, various researchers have reported that the substitution of Fe^{3+} sites with Ti^{4+} and Zr^{4+} contributes to enhancing the multiferroic properties of BFO.[28,29] Conversely, substituting Fe^{3+} with Ti^{4+} has been found to improve the electrical properties of BFO.[24] Moreover, the incorporation of 2+ ions, such as Cu^{2+}, into BFO thin films has exhibited a noteworthy reduction in leakage current and an enhancement in ferroelectric properties.[30]

Motivated by these findings, we investigated the effects of co-substituting Cu^{2+} and Ti^{4+} at the Fe^{3+} site in bulk BFO to enhance various physical properties and tailor its multifunctional performances across multiple application domains. Thus, we explored the crystal structure, vibrational and optical properties, as well as the dielectric behavior of the $BiFe_{1-x}(Ti_{1/2}Cu_{1/2})_xO_3$ system (where $x = 0$, 0.02, and 0.04, referred to respectively as BFO, $BFTCO_2$, and $BFTCO_4$). This compositional series was synthesized by the conventional solid-state reaction. Additionally, ^{57}Fe Mössbauer spectroscopy was employed as a complementary method to delve deeper into the material's characteristics.

2. Experimental details

The synthesis of polycrystalline samples derived from the $BiFe_{1-x}(Ti_{1/2}Cu_{1/2})_xO_3$ system was carried out using the standard solid-state reaction method. The substitution rates of interest in this study are $x = 0.00$, $x = 0.02$ and $x = 0.04$. High-purity Bi_2O_3, Fe_2O_3, CuO and TiO_2 oxides (Aldrich 99.9%) were accurately weighed in stoichiometric ratios using the chemical reaction equation:

$$\frac{1}{2}Bi_2O_3 + \frac{1-x}{2}Fe_2O_3 + \frac{x}{2}TiO_2 + \frac{x}{2}CuO \rightarrow BiFe_{1-x}\left(Ti_{1/2}Cu_{1/2}\right)_xO_3$$

The powder was thoroughly ground in an agate mortar for 2 hours to achieve a homogeneous mixture. Subsequently, the resulting powder was further mixed and ground for an additional 2 hours. Following this, the milled powder was pressed into pellets with a diameter of 13 mm and a thickness of 10 mm under uniaxial compaction with a load of 100 MPa for 5 minutes at RT. The pellet underwent an initial calcination at 600 °C for 2 hours. After this, the calcined pellet was ground again for 2 hours before undergoing a second calcination at 700 °C for 2 hours to achieve the desired phase formation. Following this stage, the obtained powder was ground for an additional 2 hours and pressed under 100 MPa into disks with a diameter of 8 mm and a thickness of about 1 mm. Finally, the pellets were sintered in the air using a high heating rate (250 K h^{-1}) at 880 °C for 2 hours, followed by furnace cooling at a rate of 300 K h^{-1}.

The phase purity of the synthesized samples was evaluated using an EMPYREAN X-ray diffractometer equipped with CuKα radiation ($\lambda = 1.5405$ Å, 45 kV and 30 mA) in the range of $10° \leq 2\theta \leq 80°$. Raman spectra of the sintered samples were obtained at room temperature using the LabRam HR800 from Horiba Jobin-Yvon equipped with a diode laser emitting a red line ($\lambda =$ 633 nm). UV-visible diffuse reflectance spectra of the powder samples were measured using a Thermo Scientific spectrometer model Evolution 220 (Thermo Scientific Co., Ltd., Waltham, MA, USA). Impedance measurements were carried out on gold-coated pellets using a Broadband Dielectric spectrometer. For Mössbauer spectroscopy, ^{57}Fe spectra were recorded under RT conditions using a constant acceleration spectrometer and a ^{57}Co source diffused within a rhodium matrix. Subsequent examination of the Mössbauer data was conducted through the MOSFIT software, a specialized Lorentzian line fitting program.[31]

3. Results and discussion

3.1. Structural characterization

To investigate the influence of (Ti, Cu) co-doping on the crystal structure of BFO, X-ray diffraction (XRD) measurements were performed at RT.

Fig. 1a displays the XRD patterns of BFO, $BFTCO_2$, and $BFTCO_4$ samples. From this figure, the observed high-intensity peaks suggest the phase purity and good crystalline nature of all the prepared ceramics. However, traces of a secondary phase selenite-type $Bi_{25}FeO_{40}$ were observed in both undoped and doped samples, which is a common occurrence during the solid-state synthesis of BFO-based materials, as reported in various studies.[5,32,33] Here, the detected diffraction peaks were identified with the *R3c* space group of a rhombohedral structure.[34] Furthermore, a close inspection of the patterns reveals a displacement of the peak (012) position towards lower 2θ values with an increase in Cu^{2+} and Ti^{4+} content (Fig. 1b). Presumably, this displacement can be attributed to the increase in lattice parameters. To further examine the X-ray diffraction data, Rietveld refinement of the patterns of BFO, $BFTCO_2$, and $BFTCO_4$ was performed using the FullProf program[35] to provide detailed crystal structure parameters. Here, two-phase refinements were employed to identify the amounts of the BFO phase and the $Bi_{25}FeO_{40}$ phase impurity in all prepared samples. The integrated intensity of the peaks was analyzed as a function of structural parameters using the Marquardt least-squares method to minimize differences between simulated and observed patterns. The background assessment employed the method of direct inclusion among selected background points and the minimization was performed based on parameters like

R_{wp}, R_p, R_{exp} and χ^2.[36] The profile fitting technique was adjusted according to the limit of the χ^2 function.

Fig. 2a–c illustrate the results of refinement, including the observed, calculated and difference-refined XRD patterns for BFO, $BFTCO_2$, and $BFTCO_4$ respectively. The important structural parameters, such as atomic positions, lattice parameters, bond lengths and bond angles derived from the Rietveld analysis are summarized in Table 1. As an example, we present in Fig. 2d the crystal structure of $BFTCO_2$ generated by refined ionic positions obtained from Rietveld refinement using Vesta software.

In comparison to BFO, the co-substitution was found to lead to an expansion of lattice parameters in the rhombohedral phase, consequently elevating the unit cell volume as previously observed. This augmentation can be elucidated by considering the effective ionic radii of the dopants Ti^{4+} (0.745 Å) and Cu^{2+} (0.87 Å), which are notably larger than the host ionic radius of Fe^{3+} (0.69 Å). Moreover, the increase in ionic radii of the co-dopants contributes to an augmentation in the Fe–O–Fe bond

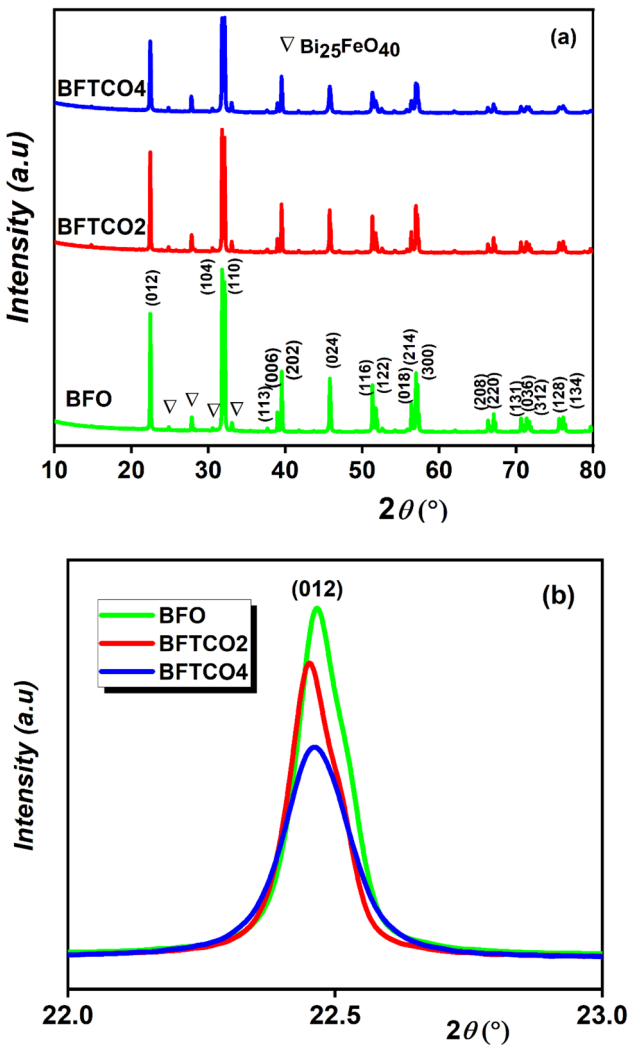

Fig. 1 XRD patterns (a) and magnified view of (012) diffraction peak (b) of BFO, $BFTCO_2$ and $BFTCO_4$ samples.

Table 1 The refined structural parameters and structure fitting factors for BFO, $BFTCO_2$ and $BFTCO_4$ ceramics

Sample	Space group	Cell (Å)	Atom	x	y	z	Percentage (%)	Bi–O (Å)	$Fe–O_1$ (Å)	$Fe–O_2$ (Å)	Fe–O–Fe (°)	R-Factors
BFO	$R3C$	$a = b = 5.5795$	Bi(6a)	0	0	0	93.16	2.331	1.915	2.144	155.26	R_p: 3.24
		$c = 13.8710$	Fe(6a)	0	0	0.2210						R_{wp}: 4.60
		$V = 373.973$	O(18b)	0.4352	0.0059	0.9537						R_{exp}: 3.41
												X^2: 1.83
$Bi_{25}FeO_{40}$	$I23$	$V = 1045.713$					6.84					
$BFTCO_2$	$R3C$	$a = b = 5.5800$	Bi(6a)	0	0	0	90.86	2.278	1.962	2.088	156.6	R_p: 2.85
		$c = 13.8720$	Fe/Ti/Cu(6a)	0	0	0.2203						R_{wp}: 4.31
		$V = 374.066$	O(18b)	0.4504	0.0187	0.9533						R_{exp}: 3.61
												X^2: 1.43
$Bi_{25}FeO_{40}$	$I23$	$V = 1046.038$					9.14					
$BFTCO_4$	$R3C$	$a = b = 5.5807$	Bi(6a)	0	0	0	90.63	2.320	1.895	2.147	157.7	R_p: 3.00
		$c = 13.8715$	Fe/Ti/Cu(6a)	0	0	0.2218						R_{wp}: 4.44
		$V = 374.146$	O(18b)	0.4457	0.0055	0.9532						R_{exp}: 3.68
												X^2: 1.46
$Bi_{25}FeO_{40}$	$I23$	$V = 1048.822$					9.37					

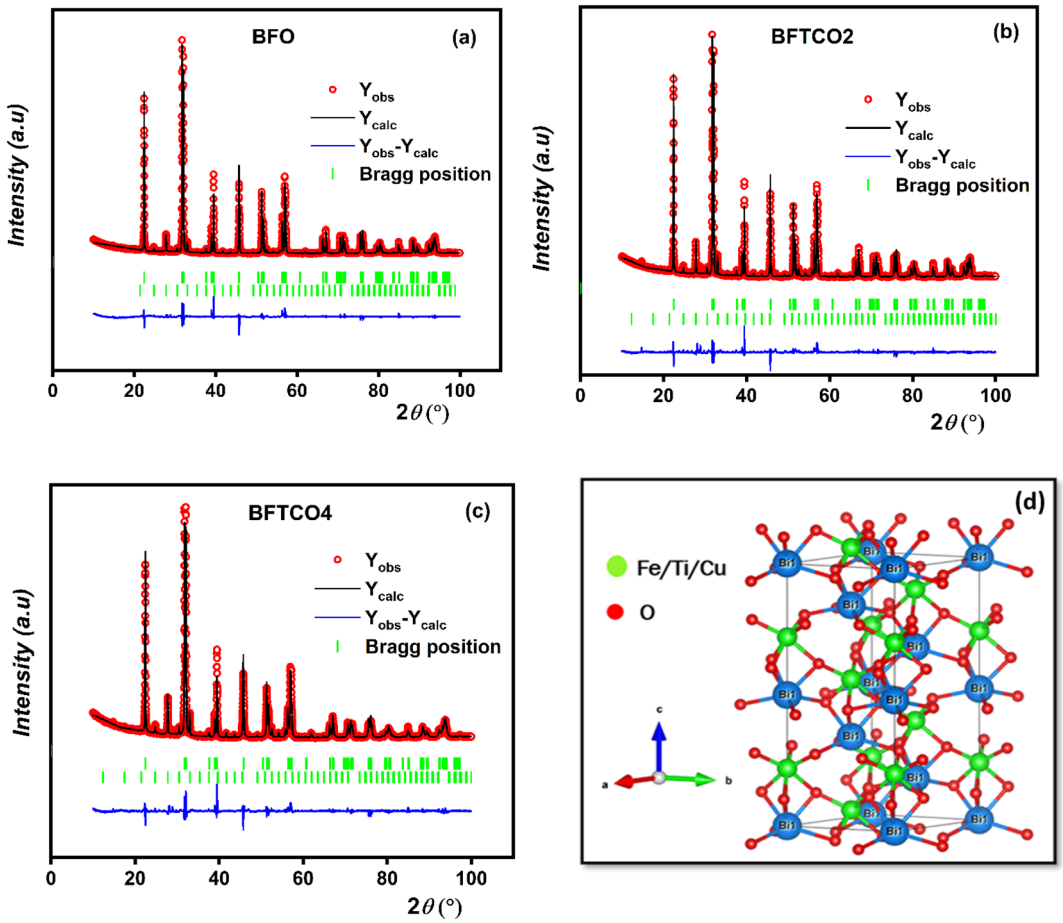

Fig. 2 Rietveld refined XRD patterns of BFO (a), $BFTCO_2$ (b) and $BFTCO_4$ (c) samples. (d) Represents the crystal structure of $BFTCO_2$ using Vesta software, employing typical cell parameters and atomic positions.

angle and induces buckling. The same deduction was observed in cobalt doping BFO nanoparticles.[37] The anticipated impact of this discovery on the magnetic characteristics of the compound was significant, as the Fe–O–Fe bond angle plays a crucial role in both superexchange and Dzyaloshinskii–Moriya (DM) interactions.[38,39]

XRD patterns are further utilized to determine the average crystallite size (D) and microstrain (ε) for BFO, $BFTCO_2$, and $BFTCO_4$ samples. D has been calculated using the Debye–Scherrer equation, described as follows:[40]

$$D = \frac{k\lambda}{\beta \cos\theta} \quad (1)$$

where β denotes the full-width at half-maximum intensity (expressed in radians), k represents a dimensionless constant with a typical value of 0.94, λ indicates the wavelength of CuKα radiation with a value of 1.5406 Å, and θ is the Bragg angle of the diffraction peak. The calculation of D is indicated in Table 2. Here D decreases from 63.1 to 50.2 nm with an increase in substitution concentration from $x = 0.0$ to $x = 0.04$. This decrease in size may be attributed to the disparate ionic radii of Cu^{2+} (0.87 Å), Ti^{4+} (0.745 Å) and Fe^{3+} (0.69 Å), resulting in lattice distortion, particularly in octahedral rotation, causing the crystal structure to contract. This interpretation finds support in the work of Rhaman *et al.*[37] Furthermore, the decrease in D can be explained by the reduction of oxygen vacancies since the motion of oxygen ions facilitates crystal growth.[41]

In this work, we aimed at the calculation of microstrain (ε) using the following relationship:[42]

$$\varepsilon = \frac{\beta}{4 \tan\theta} \quad (2)$$

where β is the line broadening at FWHM in radians, θ is the Bragg's angle in degrees, half of 2θ.

The calculated values are displayed in Table 2. Herein, ε increases from 2.08 to 2.62 $\times 10^{-3}$ with the increase of the Co-doping rate in BFO, suggesting dense and compact crystallites of doped materials. This finding is further supported by Fig. 1b,

Table 2 Average crystal size, lattice strain and bandgap energy of BFO, $BFTCO_2$ and $BFTCO_4$ samples

Samples	BFO	$BFTCO_2$	$BFTCO_4$
Crystallite size (nm)	63.1	62.3	50.2
Microstrain ε (10^{-3})	2.08	2.11	2.62
Bandgap (eV)	2.03	1.93	2

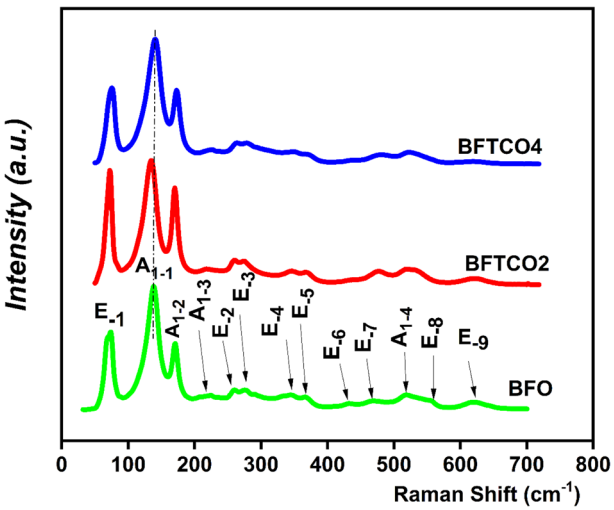

Fig. 3 The Raman spectra of the BFO, $BFTCO_2$, and $BFTCO_4$ ceramics recorded at RT.

where the shift in peak positions towards the left with the substitution rate indicates a decrease in interplanar spacing, contributing to heightened microstrain and consequently resulting in a reduction in crystallite size. A similar trend was observed in Co-substituted BFO nanoparticles,[43] as well as in BFO nanoparticles with (Cu, Zr) co-substitution.[44]

3.2. Vibrational analysis

Raman spectroscopy is a discerning approach for identifying short-range ordered structures and can detect local and static symmetries. Fig. 3 displays Raman scattering spectra of both undoped and doped BFO ceramics using an excitation wavelength of 633 nm performed at RT. According to Group Theory,[45] most of the A_1 and E active Raman modes for all samples were observable, closely corresponding to those of the rhombohedral *R3c* perovskite BFO. These outcomes were consistent with the findings of the XRD analysis.

The collective results of the pure and doped BFO ceramics were derived from the $13\Gamma = 4A_1 + 9E$ Raman active modes. In this context, the letter A denotes the symmetric transformation of a molecule during rotation around the principal axis of symmetry, while the letter E represents a twofold degenerate vibration. The low-frequency A_1 modes were primarily associated with the Bi–O vibration and lattice distortion.[46] Conversely, the high frequency of E modes was predominantly attributed to

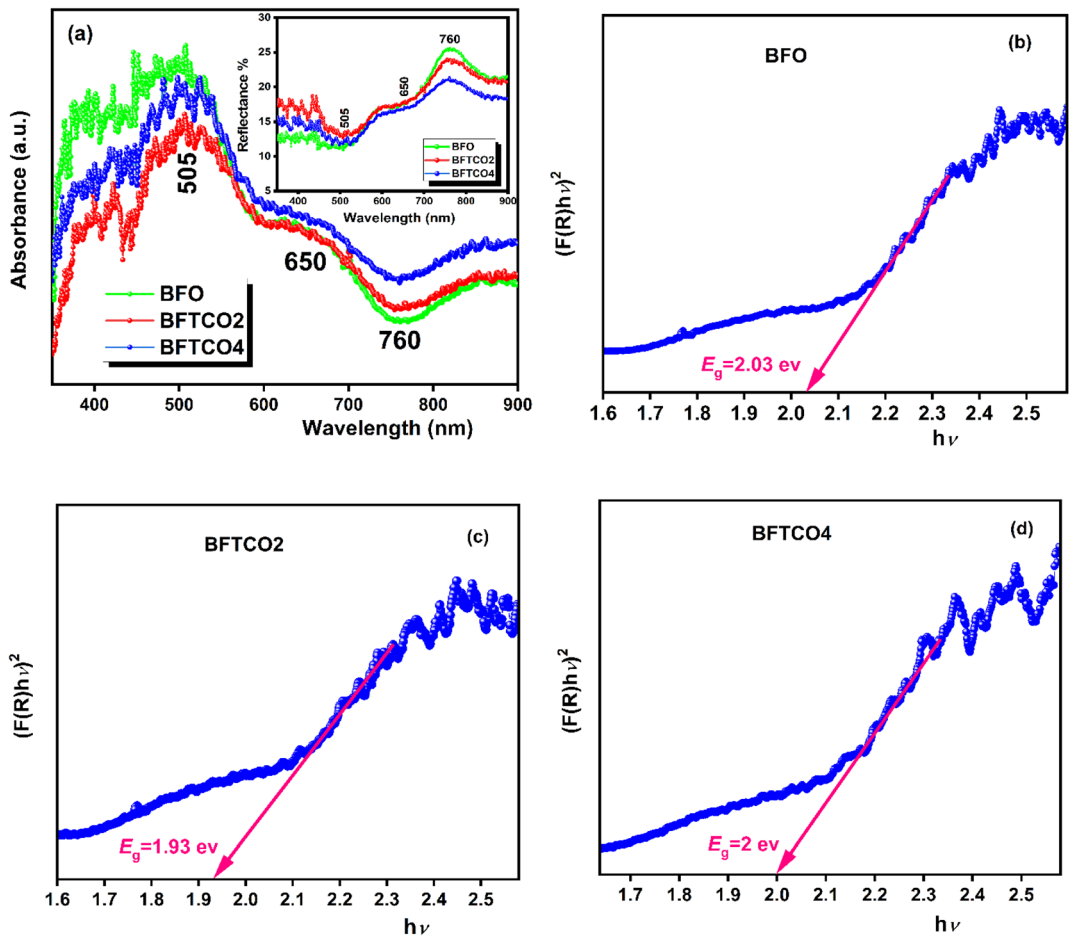

Fig. 4 a UV-visible spectra and the inset illustrates a variation of reflectance (R) as a function of wavelength. The plot of $[F(R)h\nu]^2$ Vs $h\nu$ of BFO (b), $BFTCO_2$ (c) and $BFTCO_4$ (d) samples.

the Fe–O vibration.[45] For BFO, $BFTCO_2$, and $BFTCO_4$, the higher magnitude of A_1 modes compared to E modes was due to measurements in the unpolarized configuration.[47] A_1 modes, polarized along the z-axis, were strongly excited and detectable compared to E modes polarized in the x–y plane. According to Hermet *et al.*,[48] Bi atoms contribute to low-frequency modes up to 167 cm^{-1}, while oxygen atoms dominate modes beyond 262 cm^{-1}. Moreover, Fe atoms mostly contribute to modes between 152 and 262 cm^{-1}, with potential involvement in higher frequency modes.

According to Fig. 3 and as indicated by the dashed line, we observe a slight red shift of the optical mode A_{1-1} with an increase in substitution rate up to $x = 2\%$, followed by a blue shift when the substitution rate reached $x = 4\%$. The same trend was observed in the evolution of the Bi–O bond length (deduced from the XRD study) as a function of the substitution rate. The shift bond A_{1-1} is attributed to the hybridization between Bi ($6s^2\ 6p^3$) and O ($2s^2\ 2p^4$), which is in turn related to the force constant (k) between the Bi–O bond. Therefore, the mode frequency denoted by ω can advantageously explain the shift of A_{1-1} *versus* substitution since ω is given by the following equation based on the simple harmonic mode:

$$\omega = \sqrt{\frac{k}{m^*}} = \sqrt{\frac{\propto d_{Bi-O}}{m^*}} \quad (3)$$

In this case, m^* indicates the reduced mass of optical modes. Then, eqn (3) can explain the red shift (decrease of ω) when k decreases due to the shortened Bi–O bond length, whereas the blue shift (increase of ω) occurs when the bond length increases.

3.3. Optical properties

To investigate the optical properties of BFO, $BFTCO_2$, and $BFTCO_4$, UV-vis spectroscopy measurements were carried out. Fig. 4 displays the results of these measurements taken at RT. UV-visible diffuse reflectance spectroscopy (DRS) was employed in the wavelength range of 350–900 nm, as shown in the insert in Fig. 4a. Subsequently, these UV-visible DRS spectra were converted to diffuse spectra using the Kubelka–Munk function to determine the absorption coefficient $F(R)$. Its expression is given by the following relation:

$$F(R) = \frac{(1-R)^2}{2R} \quad (4)$$

where R represents diffuse reflectance. Here, the $F(R)$ spectra are illustrated in Fig. 4a for all prepared ceramics. These illustrations showcase three absorption edges in pristine and (Ti, Cu) co-doped BFO samples. The 650 nm band stems from a metal-to-metal transition, while the approximately 760 nm band results from a crystal field transition.[49] Nevertheless, the notable absorption band observed around 505 nm is attributed to the electronic transition from the O 2p state to the Fe 3d state.[50] Hence, the energy difference between the top of the valence band (O 2p) and the bottom of the conduction band (Fe 3d) indicates the magnitude of the optical energy bandgap (E_g). Consequently, the current materials can effectively absorb light within the visible spectrum. Following this, E_g is estimated using Tauc's relation,[51] as given by the following equation:

$$F(R)hv = A(hv - E_g)^n \quad (5)$$

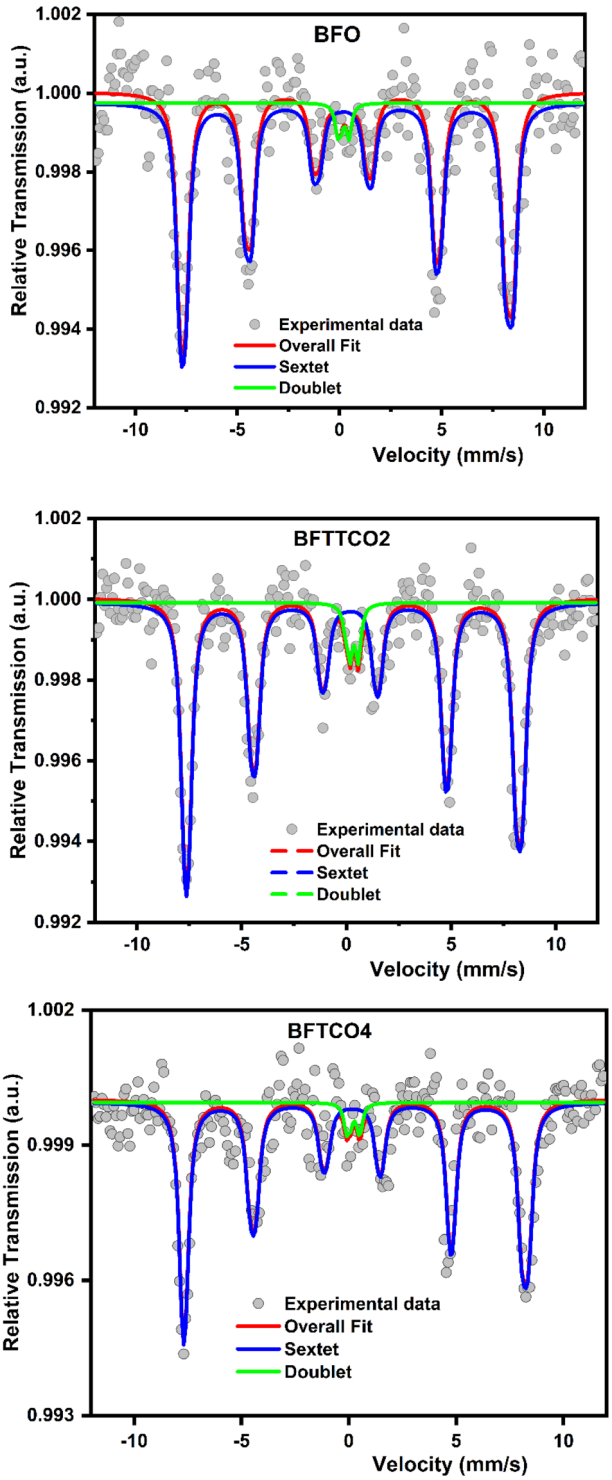

Fig. 5 Mössbauer spectra for BFO, $BFTCO_2$ and $BFTCO_4$ ceramics taken at RT.

where A is a constant, $h\nu$ indicates the photon's energy, and n characterizes the optical electronic transition process. For direct and indirect bandgap transitions, n values are 1/2 and 2, respectively. The estimation of E_g for all synthesized samples was achieved through eqn (5). Considering BFO as a direct bandgap material,[52–55] $n = 1/2$ was employed for E_g calculation. The extrapolation of the linear region in the $(F(R)\ h\nu)^2$ *versus* $h\nu$ plots, as shown in Fig. 4b–d, allowed us to estimate the values of E_g for all samples, which are tabulated in Table 2. The initial decrease in E_g for Cu and Ti co-doping BFO ceramic up to 2% can be explained by the fact that the 3d conduction band edge of Cu^{2+} ($E_{cb} = -4.96$ eV) is lower than that of Fe^{3+} ($E_{cb} = -4.78$ eV)[56] leading to the introduction of holes into the d band.[57] This phenomenon may reduce the effective energy gap between the O 2p valence band and the Fe 3d conduction band, consequently decreasing the optical band gap width of BFO. A similar discussion was carried out in the work of M. Hasan *et al.*,[58] where they demonstrated that the substitution of Fe^{3+} with manganese Mn^{4+} ($E_{cb} = -5.83$ eV) reduced the band gap width of BFO. Moreover, the Bi–O hybridization as well as the Fe–O–Fe super-transfer mechanism may also contribute to the systematic variations in the energy band gap by the substitutions, as both Fe 3d states and A-site cation states appear in the valence band and conduction band. Compared to BFO, the decrease in the Bi–O bond length indicates a stronger A–O hybridization, causing an increased orbital overlap and subsequently inducing a wider band dispersion and smaller band gap.[59] Such a reduction in band gap is consistent with previous findings on other doped BFO.[60,61] However, the increase in Bi–O bond length appears to be the main cause of the rise in E_g in the composition with $x = 4\%$ and offsets the effect of the remarkable decrease in crystallite size. Several studies have reported that the shift in bandgap in materials occurs below 10 nm due to the quantum confinement effect.[62,63] However, the crystallite size in $BFTCO_4$ is much larger and does not fall within the range affected by quantum confinement effects. Additionally, the reduced band gap of $BFTCO_2$ and $BFTCO_4$ compared to BFO makes these samples suitable candidates for photocatalytic and solar cell applications.

3.4. Mössbauer spectroscopic study

To investigate of the hyperfine magnetic behavior and oxidation state of iron atoms, ^{57}Fe Mössbauer spectroscopy was employed to analyze BFO, $BFTCO_2$, and $BFTCO_4$ ceramics. The Mössbauer spectra for these samples were recorded at RT and are visually represented in Fig. 5. The spectra for all samples exhibited a combination of a sextet (six-line) and a doublet. The sextet is attributed to the Zeeman splitting of Fe nuclear levels caused by the hyperfine magnetic field, suggesting magnetic ordering, possibly a screw or slightly canted antiferromagnetic ordering with a Néel temperature (T_N) expected to be above RT. Meanwhile, the doublet is associated with the impurity phase $Bi_{25}FeO_{40}$,[64] consistent with XRD results. The absence of a hyperfine field in the doublet indicates that the $Bi_{25}FeO_{40}$ phase does not contribute to the magnetic ordering materials. A detailed comparison of Mössbauer spectral parameters, including isomer shift IS (δ), half width at half maximum (Γ), quadrupole shift/splitting (2ε/QS), magnetic hyperfine field (B_{hf}), and fractional area, is summarized in Table 3 for BFO, $BFTCO_2$ and $BFTCO_4$ samples. Herein, the range of values of IS (δ) for all samples suggests the exclusive presence of the Fe^{3+} state, with no signal indicating the presence of Fe^{2+} ions ($0 < \delta < 0.5$ mm s^{-1} for Fe^{3+} and $0.6 < \delta < 1.4$ mm s^{-1} for Fe^{2+}).[65] Moreover, compared to the pristine BFO, the slight reduction in B_{hf} detected in $BFTCO_2$ and $BFTCO_4$ is attributed to the local distortion at Fe sites due to Bi vacancies, consistent with other reported results.[66,67] From Fig. 5, the Mössbauer spectrum of BFO exhibits evident asymmetry with a notable intensity disparity between lines 1 and 6, as well as lines 2 and 5. This asymmetry serves as compelling evidence for the presence of cycloidal modulation.[68,69] Interestingly, this asymmetry becomes slightly more symmetrical with the substitution, notably in the case of $BFTCO_2$.[69] Such a result implies that the introduction of Cu and Ti doping has the potential to disrupt the modulated spiral spin structure of BFO. A similar trend has been observed in other doped BFO compounds, including Pr-doped BFO,[70] Y-doped BFO[71] and (Zr, Zn) co-doped BFO.[26]

3.5. Dielectric measurements

To explore the dielectric properties in BFO, $BFTCO_2$, and $BFTCO_4$, an investigation was carried out on the temperature and frequency dependencies of the dielectric constant (ε'_r) and tangent loss (tan δ). Fig. 6 illustrates the temperature evolution of ε' (within the temperature range 300–675 K) for BFO (a), $BFTCO_2$ (b) and $BFTCO_4$ (c) samples at selected frequencies (ranging from 1 kHz to 1 MHz). Tan δ *versus* temperature for all samples is depicted in the inset of Fig. 6. At RT, the tan δ of BFO is approximately 0.32 when measured at 10 kHz. This value decreases in $BFTCO_2$ to around 0.13, then decreases significantly for $BFTCO_4$ to reach approximately 0.0092. Here, the

Table 3 Fit parameters obtained from Mössbauer spectroscopy investigation for BFO, $BFTCO_2$ and $BFTCO_4$ ceramics at RT

Sample	Fe site	IS (δ) (mm s^{-1})	$\Gamma/2$ (mm s^{-1})	2ε/QS (mm s^{-1})	B_{hf} (T)	Area (%)	Phase
BFO	Sextet	0.245	0.26	0.63	49.6	96	BFO
	Doublet	0.136	0.15	0.85		4	$Bi_{25}FeO_{40}$
$BFTCO_2$	Sextet	0.247	0.22	0.515	49.2	95	BFO
	Doublet	0.316	0.16	0.40		5	$Bi_{25}FeO_{40}$
$BFTCO_4$	Sextet	0.207	0.22	0.451	49.5	96	BFO
	Doublet	0.215	0.16	0.49		4	$Bi_{25}FeO_{40}$

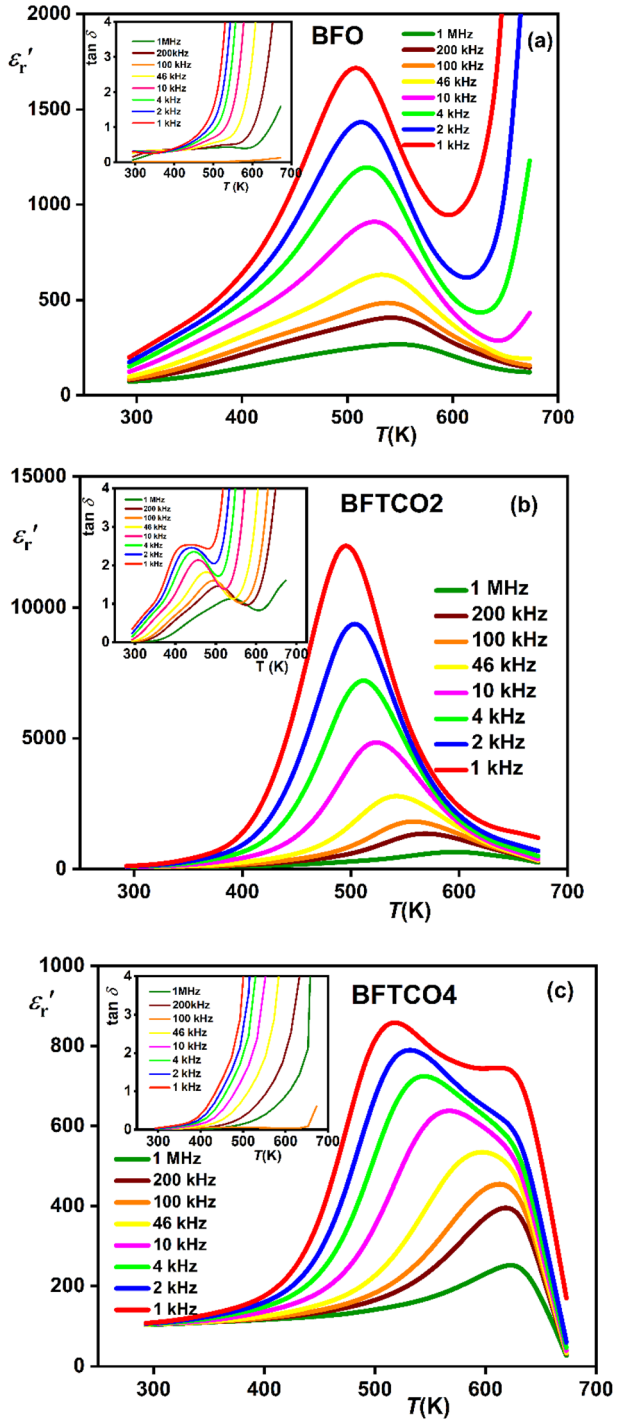

Fig. 6 Variation of ε'_r with temperature at different frequencies for BFO (a), $BFTCO_2$ (b) and $BFTCO_4$ (c). The inset shows the corresponding tan δ *versus* T.

decrease in the values of tan δ with the levels of Ti^{4+} and Cu^{2+} substitution rate reduces the conductivity of the BFO sample. This result reveals that the oxygen vacancies in substituted BFO were controlled by Cu^{2+} and Ti^{4+} doping, leading to an enhancement in its resistivity. This finding supports the earlier discussion in the structural characterization section where the decrease in average crystallite size was associated with the reduction in the amount of oxygen vacancies. Above RT and especially at elevated temperatures (>450 K), the notable rise in the value of tan δ, which decreased as the frequency increased, suggests that the hopping of electrons is unable to follow the frequencies of the applied field.

For BFO (Fig. 6a), we observed a pronounced anomaly in the dielectric constant (ε'_r) across the entire temperature range, occurring at T_m. For example, its value was 509 K detected at 1 kHz. Since the antiferromagnetic transition temperature for BFO is around (T_N) ~623–643 K,[72] indicating that the presence of this anomaly rules out magneto-electric coupling. Herein, T_m shifted towards higher temperatures as the measuring frequency rose. Additionally, the maximum dielectric permittivity (ε'_{max}) decreased as the frequency increased. All these observations confirm the relaxor-like dielectric behavior of the material. Such anomaly was observed in the work of Shama *et al.*,[73] where they attributed the relaxor behavior occurring below T_N to the presence of defects like V_{Bi}''' and $V_O^{\cdot\cdot}$ in the material. Upon doping BFO with Cu and Ti, relaxor behavior was also observed, as illustrated in Fig. 6b and c. Furthermore, to confirm the relaxor behavior, we applied the Vogel–Fulcher relationship to all prepared ceramics. This relationship is given by the following expression:[74]

$$f = f_0 \exp[-E_a/K_B(T_m - T_f)] \quad (6)$$

where f represents the applied frequency, f_0 refers to the attempt frequency, E_a indicates the activation energy, and T_f denotes the freezing temperature which corresponds to the freezing of the polar nanoregions (PNRs) dynamics in relaxor materials. The evolution of the logarithm of the frequency *versus* the inverse of T_m for pure and doped BFO ceramics is depicted in the Fig. 7 (the symbols represent the experimental data, while the solid line indicates the typical–fit curve of the Vogel–Fulcher relation). The successful fitting of the Vogel–Fulcher relation with the experimental data suggests the relaxor behavior of all compositions. The value of E_a is comparable to that found in the materials prepared by Zaho *et al.*[75] They demonstrated in its case, that achieving a long-range polar phase is difficult, which leads to a weakly coupled polar structure.

The dielectric relaxation characteristics of BFO, $BFTCO_2$, and $BFTCO_4$ ceramics can be described by two empirical parameters: γ and ΔT_{relax}. Here, γ can be calculated using the modified Curie–Weiss law, which is deduced by the following relationship:[76]

$$\frac{1}{\varepsilon'_r} - \frac{1}{\varepsilon'_{rm}} = \frac{(T - T_m)^\gamma}{C_1} \quad (7)$$

where ε'_{rm} denotes the dielectric constant maximum at T_m and C_1 is constant. γ represents the slope of the graph between $\ln\left(\frac{1}{\varepsilon'_r} - \frac{1}{\varepsilon'_{rm}}\right)$ and $\ln(T - T_m)$ (the inset in Fig. 7). ΔT_{relax} is determined by the difference between two T_m values measured at two distinct frequencies as indicated by:[77]

$$\Delta T_{relax} = T_m\,(10^5\ \text{Hz}) - T_m(10^3\ \text{Hz}). \quad (8)$$

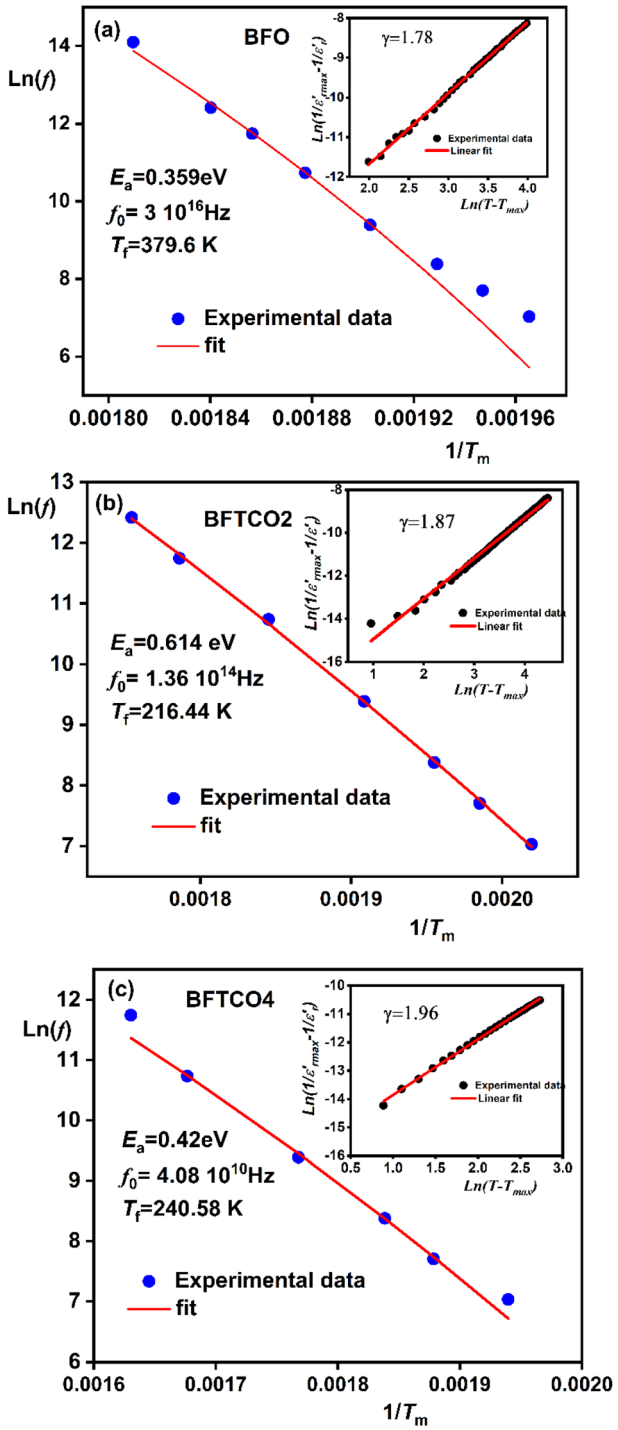

Fig. 7 Frequency dependence of T_m for BFO (a), $BFTCO_2$ (b), and $BFTCO_4$ (c) ceramics. The symbols and solid line represent data points and the fit to Vogel–Fulcher's relation, respectively. The corresponding $\ln\left(\frac{1}{\varepsilon'_r}-\frac{1}{\varepsilon'_{rm}}\right)$ plotted against $\ln(T-T_m)$ at 1 kHz is depicted in the inset.

As shown in the inset of Fig. 7, the value of the γ parameter rises with increasing x and reaches its maximum for $BFTCO_4$, with a value of 1.96. Additionally, ΔT_{relax} increases progressively with the doping level, from 30 for BFO, reaching 64 for $BFTCO_2$, and 96 for $BFTCO_4$. All these observations suggest that the substitution of Fe^{3+} by Ti^{4+} and Cu^{2+} appears to increase the random local field due to the disordered distribution created in the B site, leading to the enhancement of dielectric relaxor behavior.

For the composition $BFTCO_4$, two dielectric constant peaks appeared in the dielectric response. Similar dielectric behavior has been noted in BF-BT-based ceramics[78] and is attributed to the core–shell structure of the grains. In addition, the relaxor behavior observed in our system is certainly beneficial for energy storage performance.

4. Conclusion

To explore practical advancements and potential applications of $BiFeO_3$, especially in the field of photovoltaics and in the development of energy storage devices, we co-doped it at the Fe-site with Cu^{2+} and Ti^{4+} to form the system $BiFe_{1-x}(Ti_{1/2}Cu_{1/2})_xO_3$, with x restricted to the range of 0–0.04. These compositions were synthesized using the solid-state reaction method and the correlation between their structure, vibrational, optical and dielectric properties was highlighted. The XRD analysis revealed that substituting Cu^{2+} and Ti^{4+} at the Fe^{3+} site does not disrupt the rhombohedral structure of BFO. However, the substitution resulted in a reduction of crystallite size. On the other hand, the substitution did not prevent the formation of a secondary phase (selenite $Bi_{25}FeO_{40}$), as also identified through Mössbauer spectroscopy analysis. This study provided that Fe was present in the +3 oxidation state in pure as well as doped BFO. This is probably caused by the decrease in the formation of oxygen vacancies, which prevents the formation of Fe^{2+}. Consequently, this leads to a decrease in dielectric losses with the substitution rate of Cu and Ti as observed from the dielectric study. Optical band gap reduction due to (Ti, Cu) co-doping, as shown by the UV-vis spectroscopy results, enhanced the photocatalytic properties of BFO doping. This enhancement was facilitated by the competitive effects between the 3d conduction band edge of Cu^{2+} and the Bi–O bond length. A broad dielectric peak in the temperature-dependent dielectric constant with a pronounced frequency dispersion was observed beyond T_N, indicating relaxor behavior for all the samples. Furthermore, the degree of relaxor behavior was found to increase gradually with the doping level, attributed to the disordered distribution created in the B site. In addition, the obtained relaxor behavior might be promising for dielectric materials in various fields of application, especially for high-energy storage devices.

Author contributions

All authors participated in the preparation of the present manuscript. Material synthesis, data collection, and analysis were conducted by A. Ouertani, Z. Abdelkafi, and H. Khemakhem. Furthermore, N. Randrianantoandro assisted with the Mössbauer measurements. The initial draft of the manuscript was written by A. Ouertani with the assistance of Z. Abdelkafi and all other authors commented on the previous versions of

the manuscript. All authors read and approved the final version of the manuscript.

Conflicts of interest

The authors declare that they have no conflict of interest.

Acknowledgements

The authors acknowledge the Laboratory of Multifunctional Materials and Applications (LaMMA), (LR16ES18), Faculty of Sciences of Sfax, University of Sfax, (Tunisia).

References

1 W. Eerenstein, N. D. Mathur and J. F. Scott, *Nature*, 2006, **442**, 759–765.
2 G. Catalan and J. F. Scott, *Adv. Mater.*, 2009, **21**, 2463–2485.
3 J. Wang, J. B. Neaton, H. Zheng, V. Nagarajan, S. B. Ogale, B. Liu, D. Viehland, V. Vaithyanathan, D. G. Schlom, U. V. Waghmare, N. A. Spaldin, K. M. Rabe, M. Wuttig and R. Ramesh, *Science*, 2003, **299**, 1719–1722.
4 K. F. Wang, J.-M. Liu and Z. F. Ren, *Adv. Phys.*, 2009, **58**, 321–448.
5 T. Durga Rao, R. Ranjith and S. Asthana, *J. Appl. Phys.*, 2014, **115**, 124110.
6 C. Ederer and N. A. Spaldin, *Phys. Rev. B: Condens. Matter Mater. Phys.*, 2005, **71**, 060401.
7 V. R. Palkar, J. John and R. Pinto, *Appl. Phys. Lett.*, 2002, **80**, 1628–1630.
8 X. Chen, Y. Wu, J. Zhang and X. Chen, *Sci. China Phys. Mech. Astron.*, 2012, **55**, 404–408.
9 T. D. Rao, T. Karthik and S. Asthana, *J. Rare Earths*, 2013, **31**, 370–375.
10 T. Durga Rao, T. Karthik, A. Srinivas and S. Asthana, *Solid State Commun.*, 2012, **152**, 2071–2077.
11 F. Chang, N. Zhang, F. Yang, S. Wang and G. Song, *J. Phys. Appl. Phys.*, 2007, **40**, 7799.
12 D. H. Wang, W. C. Goh, M. Ning and C. K. Ong, *Appl. Phys. Lett.*, 2006, **88**, 212907.
13 D. Lebeugle, D. Colson, A. Forget and M. Viret, *Appl. Phys. Lett.*, 2007, **91**, 022907.
14 Y. Wang, X. Chen, H. Zhou, L. Fang, L. Liu and H. Zhang, *J. Alloys Compd.*, 2013, **551**, 365–369.
15 X. Wang, Y. Zhang, X. Song, Z. Yuan, T. Ma, Q. Zhang, C. Deng and T. Liang, *J. Eur. Ceram. Soc.*, 2012, **32**, 559–567.
16 F. Bian, S. Yan, C. Xu, Z. Liu, X. Chen, C. Mao, F. Cao, J. Bian, G. Wang and X. Dong, *J. Eur. Ceram. Soc.*, 2018, **38**, 3170–3176.
17 W. Ye, C. Zhu, Y. Xiao, X. Bai, P. Zheng, J. Zhang, W. Bai, Q. Fan, L. Zheng and Y. Zhang, *J. Eur. Ceram. Soc.*, 2023, **43**, 900–908.
18 S. Chen, T. Wang, S. Xie, J. Leng, Q. Zhu, K. Li, W. Gong, J. Zhu and Q. Wang, *ACS Appl. Mater. Interfaces*, 2024, **16**, 12521–12533.
19 S. J. Clark and J. Robertson, *Appl. Phys. Lett.*, 2007, **90**, 132903.
20 J. F. Ihlefeld, N. J. Podraza, Z. K. Liu, R. C. Rai, X. Xu, T. Heeg, Y. B. Chen, J. Li, R. W. Collins, J. L. Musfeldt, X. Q. Pan, J. Schubert, R. Ramesh and D. G. Schlom, *Appl. Phys. Lett.*, 2008, **92**, 142908.
21 T. P. Gujar, V. R. Shinde and C. D. Lokhande, *Mater. Chem. Phys.*, 2007, **103**, 142–146.
22 A. Mukherjee, Sk. M. Hossain, M. Pal and S. Basu, *Appl. Nanosci.*, 2012, **2**, 305–310.
23 N. Rong, M. Chu, Y. Tang, C. Zhang, X. Cui, H. He, Y. Zhang and P. Xiao, *J. Mater. Sci.*, 2016, **51**, 5712–5723.
24 W. Cai, C. Fu, R. Gao, W. Jiang, X. Deng and G. Chen, *J. Alloys Compd.*, 2014, **617**, 240–246.
25 A. Sathiya Priya and D. Geetha, *Braz. J. Phys.*, 2021, **51**, 40–46.
26 M. Boukhari, Z. Abdelkafi, N. Abdelmoula, H. Khemakhem and N. Randrianantoandro, *J. Mater. Sci. Mater. Electron.*, 2023, **34**, 1218.
27 J. Wu, J. Wang, D. Xiao and J. Zhu, *J. Appl. Phys.*, 2011, **109**, 124118.
28 S. Mukherjee, R. Gupta, A. Garg, V. Bansal and S. Bhargava, *J. Appl. Phys.*, 2010, **107**, 123535.
29 A. R. Jayakrishnan, B. Anina Anju, S. K. P Nair, S. Dutta and J. P. B. Silva, *J. Eur. Ceram. Soc.*, 2024, **44**, 4332–4349.
30 S. Yang, F. Zhang, X. Xie, X. Guo, L. Zhang and S. Fan, *J. Mater. Sci. Mater. Electron.*, 2017, **28**, 14944–14948.
31 R. Chakraborty, S. Mukherjee and S. Mukherjee, *J. Aust. Ceram. Soc.*, 2017, **53**, 57–65.
32 M. Ncube, D. Naidoo, K. Bharuth-Ram, D. Billing, H. Masenda, D. R. Sahu, B. K. Roul and R. M. Erasmus, *Hyperfine Interact.*, 2013, **219**, 83–88.
33 W. Ramadan and A. Gupta, *J. Nanosci. Nanotechnol.*, 2018, **18**, 7804–7810.
34 K. Chakrabarti, K. Das, B. Sarkar, S. Ghosh, S. K. De, G. Sinha and J. Lahtinen, *Appl. Phys. Lett.*, 2012, **101**, 042401.
35 A. E. Yacoubi, A. Massit, S. E. Moutaoikel, A. Rezzouk and B. C. E. Idrissi, *Am. J. Mater. Sci. Eng.*, 2017, **5**, 1–5.
36 M. Abushad, W. Khan, S. Naseem, S. Husain, M. Nadeem and A. Ansari, *Ceram. Int.*, 2019, **45**, 7437–7445.
37 M. M. Rhaman, M. A. Matin, M. N. Hossain, F. A. Mozahid, M. A. Hakim and M. F. Islam, *Bull. Mater. Sci.*, 2019, **42**, 190.
38 T. Moriya, *Phys. Rev.*, 1960, **120**, 91–98.
39 M. Salah, I. Morad, H. E. Ali, M. M. Mostafa and M. M. El-Desoky, *J. Inorg. Organomet. Polym. Mater.*, 2021, **31**, 3700–3710.
40 M. K. Anupama, B. Rudraswamy and N. Dhananjaya, *J. Alloys Compd.*, 2017, **706**, 554–561.
41 M. Kumar and K. L. Yadav, *J. Phys. Chem. Solids*, 2007, **68**, 1791–1795.
42 J.-B. Zhang, V. V. Struzhkin, W. Yang, H.-K. Mao, H.-Q. Lin, Y.-C. Ma, N.-L. Wang and X.-J. Chen, *J. Phys. Condens. Matter*, 2015, **27**, 445701.
43 M. M. Rhaman, M. A. Matin, M. N. Hossain, F. A. Mozahid, M. A. Hakim and M. F. Islam, *Bull. Mater. Sci.*, 2019, **42**, 190.
44 A. S. Priya, I. B. Shameem Banu, M. Shahid Anwar and S. Hussain, *J. Sol–Gel Sci. Technol.*, 2016, **80**, 579–586.
45 M. K. Singh, H. M. Jang, S. Ryu and M.-H. Jo, *Appl. Phys. Lett.*, 2006, **88**, 042907.

46 X. Xue, G. Tan, W. Liu and H. Ren, *Mater. Chem. Phys.*, 2014, **146**, 183–191.
47 P. Hermet, M. Goffinet, J. Kreisel and Ph. Ghosez, *Phys. Rev. B: Condens. Matter Mater. Phys.*, 2007, **75**, 220102.
48 A. Jaiswal, R. Das, T. Maity, K. Vivekanand, S. Adyanthaya and P. Poddar, *J. Phys. Chem. C*, 2010, **114**, 12432–12439.
49 X. Y. Guan, Z. W. Qiao, D. Z. Yan, Y. F. Sun and J. Li, *J. Mater. Sci. Mater. Electron.*, 2015, **26**, 6807–6813.
50 S. Kulkarni, S. Chaturvedi, R. Das and P. Poddar, *RSC Adv.*, 2015, **5**, 23563–23568, DOI: **10.1039/C5RA00933B**.
51 M. Nadeem, W. Khan, S. Khan, M. Shoeb, S. Husain and M. Mobin, *Mater. Res. Express*, 2018, **5**, 065506.
52 P. R. Vanga, R. V. Mangalaraja and M. Ashok, *Mater. Res. Bull.*, 2015, **72**, 299–305.
53 J. F. Ihlefeld, N. J. Podraza, Z. K. Liu, R. C. Rai, X. Xu, T. Heeg, Y. B. Chen, J. Li, R. W. Collins, J. L. Musfeldt, X. Q. Pan, J. Schubert, R. Ramesh and D. G. Schlom, Optical band gap of $BiFeO_3$ grown by molecular-beam epitaxy, *Appl. Phys. Lett.*, 2008, **92**, 142908, **https://pubs.aip.org/aip/apl/article-abstract/92/14/142908/166239/Optical-band-gap-of-BiFeO3-grown-by-molecular-beam?redirectedFrom=fulltext**.
54 Y. Xu and M. Shen, *Mater. Lett.*, 2008, **62**, 3600–3602.
55 A. Manzoor, A. M. Afzal, N. Amin, M. I. Arshad, M. Usman, M. N. Rasool and M. F. Khan, *Ceram. Int.*, 2016, **42**, 11447–11452.
56 Y. Xu and M. A. A. Schoonen, *Am. Mineral.*, 2000, **85**, 543–556.
57 J. Rodríguez-Carvajal, M. Hennion, F. Moussa, A. H. Moudden, L. Pinsard and A. Revcolevschi, *Phys. Rev. B: Condens. Matter Mater. Phys.*, 1998, **57**, R3189–R3192.
58 M. Hasan, M. A. Basith, M. A. Zubair, Md. S. Hossain, R. Mahbub, M. A. Hakim and Md. F. Islam, *J. Alloys Compd.*, 2016, **687**, 701–706.
59 Z. Zhang, P. Wu, L. Chen and J. Wang, *Appl. Phys. Lett.*, 2010, **96**, 012905.
60 S. Irfan, Y. Shen, S. Rizwan, H.-C. Wang, S. B. Khan and C.-W. Nan, *J. Am. Ceram. Soc.*, 2017, **100**, 31–40.
61 S. Hussain and S. K. Hasanain, *J. Alloys Compd.*, 2016, **688**, 1151–1156.
62 S. K. Patra, B. Bhushan and A. Priyam, *Dalton Trans.*, 2016, **45**, 3918–3926.
63 C. Li, B. Dong and Q. Wang, in *Handbook of Nanomaterials Properties*, ed. B. Bhushan, D. Luo, S. R. Schricker, W. Sigmund and S. Zauscher, Springer, Berlin, Heidelberg, 2014, pp. 1263–1298.
64 J. Li, H. He, F. Lü, Y. Duan and D. Song, *MRS Online Proc. Libr. OPL*, 2001, **676**, Y7.7.
65 C. Janot, in *Colloquium Spectroscopicum Internationale*, ed. J. P. Robin, Pergamon, 1976, pp. 53–64.
66 J. Prado-Gonjal, D. Ávila, M. E. Villafuerte-Castrejón, F. González-García, L. Fuentes, R. W. Gómez, J. L. Pérez-Mazariego, V. Marquina and E. Morán, *Solid State Sci.*, 2011, **13**, 2030–2036.
67 T. R. Paudel, S. S. Jaswal and E. Y. Tsymbal, *Phys. Rev. B: Condens. Matter Mater. Phys.*, 2012, **85**, 104409.
68 S. R. Burns, O. Paull, J. Juraszek, V. Nagarajan and D. Sando, *Adv. Mater.*, 2020, **32**, 2003711.
69 A. Agbelele, D. Sando, C. Toulouse, C. Paillard, R. D. Johnson, R. Ruffer, A. F. Popkov, C. Carretero, P. Rovillain, J.-M. L. Breton, B. Dkhil, M. Cazayous, Y. Gallais, M.-A. Measson, A. Sacuto, P. Manuel, A. K. Zvezdin, A. Barthelemy, J. Juraszek and M. Bibes, *Adv. Mater.*, 2017, **29**, 1602327.
70 S. Kumar Srivastav, N. S. Gajbhiye and A. Banerjee, *J. Appl. Phys.*, 2013, **113**, 203917.
71 H. Fki, M. Koubaa, L. Sicard, W. Cheikhrouhou-Koubaa, A. Cheikhrouhou and S. Ammar-Merah, *Ceram. Int.*, 2017, **43**, 4139–4150.
72 P. Fischer, M. Polomska, I. Sosnowska and M. Szymanski, *J. Phys. C Solid State Phys.*, 1980, **13**, 1931.
73 S. Sharma, J. M. Siqueiros and O. R. Herrera, *J. Alloys Compd.*, 2021, **853**, 156979.
74 D. Viehland, S. J. Jang, L. E. Cross and M. Wuttig, *J. Appl. Phys.*, 1990, **68**, 2916–2921.
75 J. Zhao, T. Hu, Z. Fu, Z. Pan, L. Tang, X. Chen, H. Li, J. Hu, L. Lv, Z. Zhou, J. Liu, P. Li and J. Zhai, *Small*, 2023, **19**, 2206840.
76 K. Uchino and S. Nomura, *Ferroelectrics*, 1982, **44**, 55–61.
77 D. Zheng, R. Zuo, D. Zhang and Y. Li, *J. Am. Ceram. Soc.*, 2015, **98**, 2692–2695.
78 Z. Chen, X. Bu, B. Ruan, J. Du, P. Zheng, L. Li, F. Wen, W. Bai, W. Wu, L. Zheng and Y. Zhang, *J. Eur. Ceram. Soc.*, 2020, **40**, 5450–5457.